

Impact of mass concentration variations on plasma dynamics in a laser-ablated CH target

Hafiz Muhammad Siddique, Guannan Zheng(郑冠男), Tao Tao(陶弢), Xiao-Bao Jia(贾晓宝), and Jian Zheng(郑坚)
Citation: Chin. Phys. B, 2025, 34 (**11**): 115203. DOI: 10.1088/1674-1056/addcd0
Chttp://cpb.iphy.ac.cn; http://iopscience.iop.org/cpb

What follows is a list of articles you may be interested in

Diagnosis of electron temperature of copper foil plasmas produced at the Shenguang-II facility

Chenglong Zhang(张成龙), Haochen Gu(谷昊琛), Yu Dai(戴羽), Ke Fang(方可), Yufeng Dong(董玉峰), Peng Zhou(周鹏), and Yingjun Li(李英骏)
Chin. Phys. B, 2025, 34 (**7**): 075202. DOI: 10.1088/1674-1056/adca19

Time-resolved *K*-shell x-ray spectra of nanosecond laser-produced titanium tracer in gold plasmas

Zhencen He(何贞岑), Jiyan Zhang(张继彦), Jiamin Yang(杨家敏), Bing Yan(闫冰), and Zhimin Hu(胡智民)
Chin. Phys. B, 2023, 32 (**1**): 015202. DOI: 10.1088/1674-1056/ac8e95

Hot-electron deposition and implosion mechanisms within electron shock ignition

Wan-Li Shang(尚万里)†, Xing-Sen Che(车兴森), Ao Sun(孙奥), Hua-Bing Du(杜华冰), Guo-Hong Yang(杨国洪), Min-Xi Wei(韦敏习), Li-Fei Hou(侯立飞), Yi-Meng Yang(杨轶濛), Wen-Hai Zhang(张文海), Shao-Yong Tu(涂绍勇), Feng Wang(王峰), Hai-En He(何海恩), Jia-Min Yang(杨家敏), Shao-En Jiang(江少恩), and Bao-Han Zhang(张保汉)
Chin. Phys. B, 2020, 29 (**10**): 105201. DOI: 10.1088/1674-1056/aba9c3

Measurement of molybdenum ion density for L-mode and H-mode plasma discharges in the EAST tokamak

Yongcai Shen(沈永才), Hongming Zhang(张洪明), Bo Lyu(吕波), Yingying Li(李颖颖), Jia Fu(符佳), Fudi Wang(王福地), Qing Zang(臧庆), Baonian Wan(万宝年), Pan Pan(潘盼), Minyou Ye(叶民友)
Chin. Phys. B, 2020, 29 (**6**): 065206. DOI: 10.1088/1674-1056/ab8456

A new ignition hohlraum design for indirect-drive inertial confinement fusion

Xin Li(李欣), Chang-Shu Wu(吴畅书), Zhen-Sheng Dai(戴振生), Wu-Di Zheng(郑无敌), Jian-Fa Gu(谷建法), Pei-Jun Gu(古培俊), Shi-Yang Zou(邹士阳), Jie Liu(刘杰), Shao-Ping Zhu(朱少平)
Chin. Phys. B, 2016, 25 (**8**): 085202. DOI: 10.1088/1674-1056/25/8/085202

Impact of mass concentration variations on plasma dynamics in a laser-ablated CH target

Hafiz Muhammad Siddique[1,2], Guannan Zheng(郑冠男)[1,2], Tao Tao(陶弢)[1,2], Xiao-Bao Jia(贾晓宝)[1,2], and Jian Zheng(郑坚)[1,2,3,†]

[1] *Department of Plasma Physics and Fusion Engineering, University of Science and Technology of China, Hefei* 230026, *China*
[2] *Chinese Academy of Sciences (CAS) Key Laboratory of Frontier Physics in Controlled Nuclear Fusion, University of Science and Technology of China, Hefei* 230026, *China*
[3] *Collaborative Innovation Center of IFSA, Shanghai Jiao Tong University, Shanghai* 200240, *China*

(Received 9 March 2025; revised manuscript received 29 April 2025; accepted manuscript online 26 May 2025)

Laser-produced plasmas in the field of inertial confinement fusion usually consist of multiple ion species with different atomic numbers and charge-to-mass ratios. With the presence of various plasma gradients, ion diffusion is driven, causing ion concentration to evolve and deviate from its initial value. In order to investigate the effect of ion diffusion on laser-produced plasmas, we implement an ion diffusion module within the radiation-hydro code MULTI-1D [*Comput. Phys. Commun.* **203** 226 (2016)]. Under the planar target geometry and simulation parameters considered in this study, ion species separation primarily occurs near ablation front and underdense region. Although ion diffusion just has a slight impact on plasma hydrodynamics such as density, temperature and pressure profiles, it could have significant influence on the processes in relevant to ion-acoustic wave, whose damping rate depends sensitively on ion concentration. It is found that the coupling factor of cross-beam energy transfer (CBET) could change a lot when ion diffusion is taken into account, indicating that ion diffusion could play important role in laser fusion.

Keywords: mass diffusion, ion transport, species separation, hydrodynamic simulation

PACS: 52.57.–z, 52.38.–r, 52.25.Dg, 52.30.Ex

DOI: 10.1088/1674-1056/addcd0 **CSTR:** 32038.14.CPB.addcd0

1. Introduction

Laser-produced plasmas usually consist of multiple ion species. In the field of inertial confinement fusion (ICF),[1] both fuel and ablation shell are made of mixture matter: the former is DT and the latter could be CH or doped high density carbon.[2–4] During implosion, intense thermodynamic forces such as pressure and temperature gradients, can induce inter-species diffusion,[5,6] leading to ion species separation, which means that ion-species concentration is not a constant but evolves with space and time.

On the other hand, ion-species concentration can profoundly affect laser-produced plasmas through various aspects. Since plasma opacity depends on ion-species concentration, the Rayleigh–Taylor instability can be mitigated via properly doping ablation shell.[7–9] Since ion-acoustic waves sensitively depend on ion-species concentration,[10] stimulated Brilloun scattering can be suppressed by increased Landau damping in multiple-ion-species hohlraum plasmas.[11] The cross-beam energy transfer (CBET) is one of the key techniques for controlling compression symmetry in ignition experiments,[12,13] and it also exhibits strong sensitivity to ion-species concentration.[14,15] This sensitivity arises because CBET, mediated by the ion-acoustic wave (IAW), depends critically on the IAW damping rate. Since different ion species modify the Landau damping rate, ion-species separation should be self-consistently taken into account in the study of laser-produced multiple-ion plasmas.

The radiation hydrodynamic simulation is necessary in the fields of ICF and high energy density physics. Simulation codes are developed to solve a set of fundamental equations, including the continuity equation, the momentum equation, the energy equations, with tabulated equation of state (EOS), and opacity data. However, there are radiation hydrodynamic codes which simulate the dynamic states of matter throughout the ICF process but do not take into account the evolution of ion-species concentration, such as MULTI-1D.[16,17] Such simplifications overlook certain plasma evolution characteristics, such as ion-species separation at the interface between the DT fuel and CH plastic layers.[18–20] Incorporating the effects of ion-species separation into advanced radiation hydrodynamic models, such as the MULTI-1D framework,[16] could enhance the simulation accuracy in ICF and enable us to evaluate the impacts of ion-species separation on implosion dynamics.

In this article, we take into account of ion-species separation in radiation hydrodynamic simulation by integrating ion diffusion equations[21,22] within the framework of MULTI-1D. For the sake of self-consistency, the equations of state (EOS) are also modified to depend on ion-species concentration. Under laser-plasma conditions, energy transport is predominantly

†Corresponding author. E-mail: jzheng@ustc.edu.cn

© 2025 Chinese Physical Society and IOP Publishing Ltd. All rights, including for text and data mining, AI training, and similar technologies, are reserved.

governed by electron thermal conduction as also reported by Ramis *et al*., in MULTI-1D,[16] while the contribution from ions is relatively minor, so we have ignored the enthalpy due to ions diffusion. In our simulation conditions, it is found that plasma hydrodynamics differ a little with or without inclusion of ion diffusion process. However, the ion-species concentration notably deviates from initial value, and thus can have significant impact on CBET factor. The article is organized as follows. In Section 2, we present the framework for calculating two-ion species flux and the associated diffusion coefficients, laying the foundation for understanding their role in plasma dynamics. Subsection 3.1 details the implementation of the modified equations into the MULTI-1D hydrodynamic simulation framework, highlighting the adaptations required for accurately modeling ion-species concentration effects and key modifications in the MULTI-1D code for better understanding. In Subsections 3.2 and 3.3, we discuss the results obtained from these modifications, including a comprehensive analysis of the impact of the enhanced two-ion treatment on plasma properties under various conditions. Finally, we conclude in Section 4 with a summary of the key findings and their implications for laser-driven inertial confinement fusion research.

2. Two-ion species flux and diffusion coefficients

In two-ion species plasma, we denote the light ion species as a and the heavy species as b. The mass diffusion flux of the component a is defined as[22]

$$\boldsymbol{i}_a = \rho_a(\boldsymbol{u}_a - \boldsymbol{u}), \tag{1}$$

where ρ_a and $\boldsymbol{u}_a$ are the mass density and flow velocity of species a, $\boldsymbol{u}$ is the velocity of the bulk fluid defined as

$$\boldsymbol{u} = \frac{\rho_a \boldsymbol{u}_a + \rho_b \boldsymbol{u}_b}{\rho}, \tag{2}$$

where $\rho = \rho_a + \rho_b$ is the total mass density of the fluid. Obviously, the mass diffusion flux satisfies the condition $\boldsymbol{i}_a + \boldsymbol{i}_b = 0$. Applying the conservation of mass equation to each species a, it is straightforward to obtain the evolution equation for the mass concentration c_a of component a,

$$\frac{\rho \partial c_a}{\partial t} + \rho \boldsymbol{u} \cdot \nabla c_a + \nabla \cdot \boldsymbol{i}_a = 0, \tag{3}$$

where $c_a = \rho_a/\rho$ and satisfies the condition $c_a + c_b = 1$. In one-dimensional (1D) Lagrangian coordinate, equation (3) can be simplified as

$$\frac{\partial c_a}{\partial t} + \frac{\partial i_a}{\partial m} = 0, \tag{4}$$

where m is Lagrangian coordinate of areal mass density. The diffusion flux is driven by plasma inhomogeneity, and is proportional to plasma gradients in the case of local quasi-equilibrium,

$$i_a = -A^2 \rho^2 D \left[\frac{\partial c_a}{\partial m} + k_P^{(\mathrm{i})} \frac{\partial \ln P_\mathrm{i}}{\partial m} + k_T^{(\mathrm{i})} \frac{\partial \ln T_\mathrm{i}}{\partial m} + k_T^{(\mathrm{e})} \frac{\partial \ln T_\mathrm{e}}{\partial m} + \frac{e k_\mathrm{E}}{T_\mathrm{i}} \frac{\partial \phi}{\partial m} \right], \tag{5}$$

where A is a geometric factor which equals to 1 in planar configuration, D is the classical diffusion coefficient, $P_\mathrm{i} = P_a + P_b = nT_\mathrm{i}$ is the total ion pressure, $P_{a,b}$ are the pressures of species a and b, $n = n_a + n_b$ is the total ion number density, $n_{a,b}$ are the ion number densities of species a and b, and T_i is the ion temperature. The first term in the brackets on the right side of Eq. (5) represents the classical diffusion flux produced by the mass concentration gradient, and the remaining terms are the ion thermal pressure diffusion flux, ion thermal diffusion flux, electron thermal diffusion flux and the electro diffusion flux, respectively. The static electric field in Eq. (5) is self-generated, and is proportional to electron gradients,

$$\frac{\partial \phi}{\partial m} = \frac{1}{e n_\mathrm{e}} \left(\frac{\partial P_\mathrm{e}}{\partial m} + \frac{\eta_\mathrm{e} T_\mathrm{e}}{e} \frac{\partial \ln T_\mathrm{e}}{\partial m} \right), \tag{6}$$

where e is the elementary charge, n_e is the electron number density, P_e and T_e are electron pressure and temperature respectively. η_e is the thermal force coefficient given by[22]

$$\eta_\mathrm{e} \approx \frac{0.47 + 0.94(Z^*)^{-1}}{0.31 + 1.20(Z^*)^{-1} + 0.41(Z^*)^{-2}}, \tag{7}$$

where Z^* is the average ion charge state,

$$Z^* = \frac{(c_a/m_a)Z_a^2 + (c_b/m_b)Z_b^2}{(c_a/m_a)Z_a + (c_b/m_b)Z_b}.$$

Here $Z_{a,b}$ are the charge states of species a and b.

The diffusion coefficients D, $k_P^{(\mathrm{i})}$, $k_T^{(\mathrm{i})}$, $k_T^{(\mathrm{e})}$, and k_E can be obtained by kinetic theory.[21] The classical diffusion coefficient D is given by

$$D = \frac{\rho T_\mathrm{i}}{A_{ab} \mu_{ab} n_a \nu_{ab}} \frac{c_a c_b}{c_a m_b + c_b m_a}. \tag{8}$$

Here $m_{a,b}$ are the ion masses of species a and b, $\mu_{ab} = m_a m_b/(m_a + m_b)$ is the reduced ion mass, ν_{ab} is the collision frequency between a and b defined as

$$\nu_{ab} = \frac{4\sqrt{2\pi}}{3} \frac{n_b Z_a^2 Z_b^2 e^4 \ln \Lambda_{ab}}{\sqrt{\mu_{ab}} T_\mathrm{i}^{3/2}}, \tag{9}$$

where $\ln \Lambda_{ab}$ is the Coulomb logarithm

$$\ln \Lambda_{ab} = 23 - \ln \left(Z_a Z_b \cdot \frac{\sqrt{n_a Z_a^2 + n_b Z_b^2}}{T_\mathrm{i}^{3/2}} \right), \quad \ln \Lambda_{ab} \geq 1. \tag{10}$$

And A_{ab} is the kinetic friction coefficient for ion species a and b given by

$$A_{ab} = -\frac{1}{g_0^{(a)}} \frac{(1+m_b/m_a)^{1/2} c_b (c_b/c_a + m_b/m_a)}{(m_b/m_a)^{3/2}}. \tag{11}$$

The other four diffision coefficients are given by

$$k_P^{(\mathrm{i})} = c_a c_b (m_b - m_a) \left(\frac{c_a}{m_a} + \frac{c_b}{m_b} \right), \tag{12a}$$

$$k_T^{(\mathrm{i})} = \frac{h_0^{(a)}}{g_0^{(a)}} m_a m_b \left(\frac{c_a}{m_a} + \frac{c_b}{m_b} \right)^2, \tag{12b}$$

$$k_T^{(\mathrm{e})} = -m_a m_b c_a c_b \left(\frac{c_a}{m_a} + \frac{c_b}{m_b} \right) \left(\frac{Z_a^2}{m_a} - \frac{Z_b^2}{m_b} \right) \frac{\eta_\mathrm{e} T_\mathrm{e}}{Z^* T_\mathrm{i}}, \tag{12c}$$

$$k_\mathrm{E} = m_a m_b c_a c_b \left(\frac{c_a}{m_a} + \frac{c_b}{m_b} \right) \left(\frac{Z_a}{m_a} - \frac{Z_b}{m_b} \right). \tag{12d}$$

The factors $g_0^{(a)}$ and $h_0^{(a)}$ are given in Appendix B.

3. Hydrodynamic simulations with the inclusion of diffusion model

The equations (4)–(12) describe the ion diffusion processes. In this section, we provide a concise overview of the key modifications and the integration of a new subroutine for ion mass diffusion equations into the MULTI-1D framework. Additionally, we present a comparative analysis of the simulation results, evaluating the updated model against the previous version. This analysis offers insights into the effectiveness of the new model and its potential applications in plasma physics simulations.

3.1. Integration of ion diffusion equations into MULTI-1D

MULTI-1D is a specialized 1D radiation hydrodynamics program designed for studying ICF. It treats the plasma as a single fluid from the perspective of ion separation and does not include a physics module for the separation of components. In this method, MULTI-1D follows the Lagrangian coordinate system, where the fluid elements move with the grid, maintaining a constant mass. In our modified version of the Multi-IFE code, significant advancements have been made, especially by introducing a new subroutine named `mass_concentration` to handle the ion mass diffusion phenomenon which was missing in the previous version.

Our approach employs species-specific EOS and ionization tables generated using FEOS[23] and opacity tables by TOPS.[24] In the MULTI-1D program, equations (4) and (5) are solved in the new subroutine `mass_concentration`. The evolution of the mass concentration c_a is determined by plasma data and the control Eqs. (4) and (5). Additionally, c_a should impact the simulation results of MULTI-1D and to account for this process, we have corrected the equations of state (EOS) data, making EOS function of ion mass concentration c_a,

$$P_\mathrm{i} = P_\mathrm{i}(\rho, e_\mathrm{i}, c_a), \quad T_\mathrm{i} = T_\mathrm{i}(\rho, e_\mathrm{i}, c_a),$$

$$P_\mathrm{e} = P_\mathrm{e}(\rho, e_\mathrm{e}, c_a), \quad T_\mathrm{e} = T_\mathrm{e}(\rho, e_\mathrm{e}, c_a).$$

For high-level modifications involving EOS data, the local linearization method is applied and in addition, $\partial P/\partial c = \partial P/\partial c\,(\rho, e, c_0)$, and $\partial T/\partial c = \partial T/\partial c\,(\rho, e, c_0)$ derivatives are also used. Here ρ, e, and c_0 refer to the discrete density, internal energy and initial mass concentration respectively, where c_a is the mass concentration vector. Assuming that c_a does not deviate too far from c_0 (initial value), according to Eqs. (3) and (4) the modified general expression for pressure and temperature can be expressed in terms of f as follows:

$$f(\rho, e, c_a) = f(\rho, e, c_0) + (c_a - c_0) \frac{\partial f}{\partial c}(\rho, e, c_0). \tag{13}$$

Equation (13) is implemented in the subroutine `mass_concentration`, where the physical effects of mass concentration separation are introduced into the MULTI-1D program. In the loop process, each sub-step first obtains the uncorrected $P(\rho, e, c_0)$ and $T(\rho, e, c_0)$ and the corresponding local partial derivative data $\partial P/\partial c\,(\rho, e, c_0)$ and $\partial T/\partial c\,(\rho, e, c_0)$ according to the plasma state quantity (ρ, e). This process is carried out in `mass_concentration`, and then the evolution of c_a or c_b will be solved in `mass_concentration`, and the thermodynamic state quantities P and T will be corrected according to the simulation results and using updated formula (12). The corrected state quantities for temperatures and pressures will participate in subsequent calculations. The MULTI-1D code flow of the component separation physics module is shown in Fig. 1.

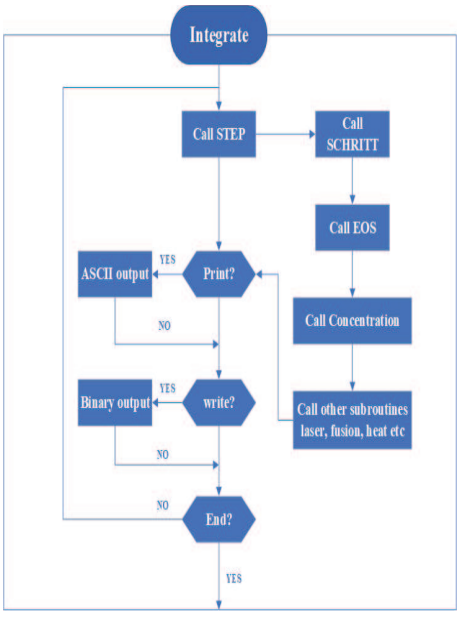


Fig. 1. Modified integration subroutine (schritt).

The relative error $(|M_a - \overline{M_a}|/\overline{M_a})$ in total mass of the ion species a, $M_a = \int c_a \,\mathrm{d}m$, is plotted over time (0 ns–3 ns) to validate numerical accuracy as shown in Fig. 2. The error remains tightly bound within < 1 ppm (parts per million), demonstrating exceptional conservation of M_a with negligible deviations showcasing the robustness of the numerical method.

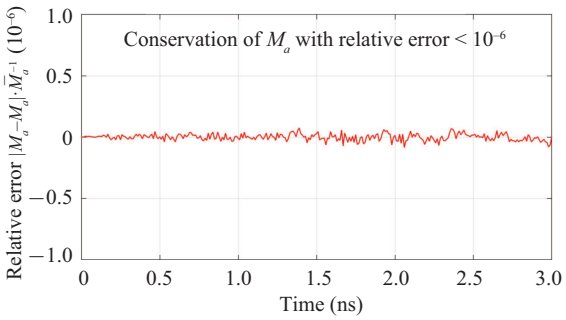


Fig. 2. Relative error in mass conservation (M_a) showing less than 1 ppm variation over 3 ns.

As mentioned earlier, we have used the opacity tables from TOPS for the respective elements, but in the current version we are not considering the impact of the mass concentration on opacity and only the correction of the EOS data by the change in abundance of ion components has been realized. Further details about the numerical implementation of our model is given in Appendix A.

3.2. Ion diffusion and hydrodynamic results

The MULTI-1D program was used to simulate the implosion process of a laser-irradiated planar CH target. Figure 3 depicts the laser pulse power as a function of time. The laser operates with a square pulse profile where the power abruptly rises to its maximum value of 200 TW at 0.05 ns, remains constant for a period of 2 ns, and then rapidly drops back to zero. This pulse is often used in simulations to represent a uniform and instantaneous energy delivery to a target. The total simulation time is 3 ns. The initial target density is 1.06 g/cm^3 with initial ion and electron temperature of 0.1 eV. Further, the target consists of a 200-μm thick plastic (CH) with planar geometry. The laser operates at a wavelength of 351 nm, delivering a peak energy of 399.1 kJ at a maximum intensity of 2×10^{14} W/cm^2.

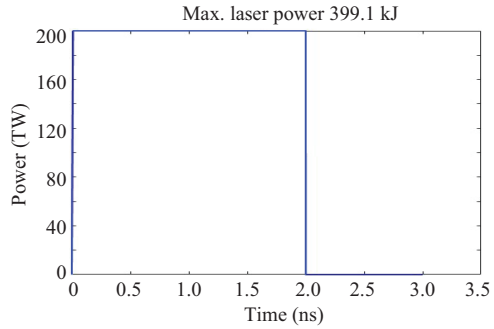


Fig. 3. Laser pulse shape in the simulation.

Figure 4 illustrates the variation of mass density ρ and hydrogen ion concentration c_a with respect to the target thickness XC at $t = 0.49$ ns for a CH target. The mass density ρ, shown on the left y-axis in blue in Fig. 3(a), rises sharply around $XC \approx 170$ μm, that corresponds to the formation of a laser-driven ablation front, that propagates into the cold dense CH target. As the laser energy heats the target material, intense energy deposition occurs near the ablation front. From Eq. (5), the laser deposition causes a steep temperature and density gradients along with the pressure gradient that compresses the material in the ablation region. Then density drops steeply to nearly zero beyond $XC \approx 200$ μm, as the ablation process leads to a steep decrease in density because the material transitions into a plasma state and rapidly expands outward into the lower-density region. The hydrogen ion concentration c_a, plotted on the right y-axis in red, remains constant in the core, and sharply rises after laser deposition on the target due to large temperature, pressure and electro gradients as shown in the Fig. 4(b). The concentration decreases near $XC \approx 170$ μm, and gradually declines beyond $XC \approx 200$ μm. The spatial distribution of the normalized electron number density, n_e/n_{cr} as a function of target thickness at $t = 1.99$ ns can also be seen. The electron number density exhibits a rapid decline beyond the ablation region, with a peak near the critical surface $n_e = n_{cr}$ due to the transition of the dense inner plasma into an expanding, lower-density region. The sharp drop in n_e/n_{cr} near the ablation surface reflects the rarefaction wave propagating outward, leading to plasma expansion and density stratification. We can see that the after a sharp decline in hydrogen ion concentration with plasma expansion, the concentration later again rises due to high baro, thermo-, and electro-gradients in the coronal region. The hydrogen ion concentration peaks mainly close to the ablation front. With the evolution of time, the plasma in the coronal region continues to diffuse outward, a small amount of H ions will tend to diffuse toward the ablation surface, and more H ions will diffuse toward the vacuum.

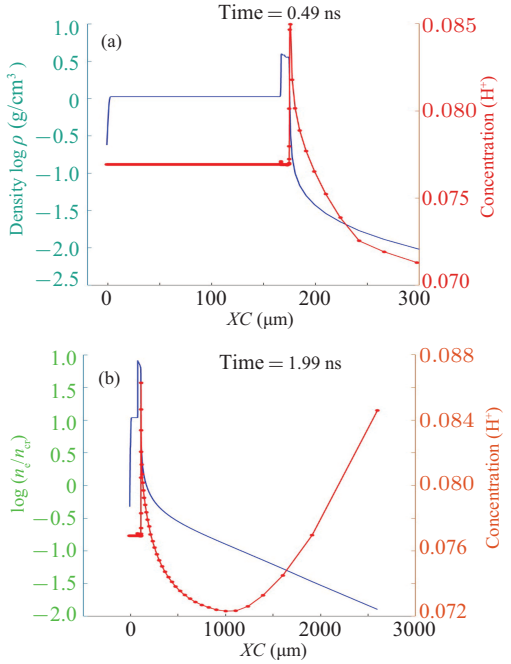


Fig. 4. Spatial distribution of density and hydrogen concentration.

We compare in Fig. 5 the diffusion coefficients k_E (red solid line), $k_P^{(i)}$ (blue dashed line), $k_T^{(i)}$ (green dash-dot line), $k_T^{(e)}$ (magenta dotted line) for hydrogen ions at two different

time frames. Each coefficient corresponds to a specific physical effect: k_{E} for electro-diffusion, $k_P^{(\mathrm{i})}$ for baro-diffusion, $k_T^{(\mathrm{i})}$ for thermo-diffusion for ions, and $k_T^{(\mathrm{e})}$ shows the thermo-diffusion for electrons. The ion thermal diffusion coefficient, $k_T^{(\mathrm{i})}$, exhibits an initial peak at ~ 0.4 ns of the laser pulse, surpassing all other diffusion coefficients. However, as the system evolves, the electron thermal diffusion coefficient, $k_T^{(\mathrm{e})}$, gradually increases and reaches its maximum around $\sim$ 2 ns, exceeding the earlier peak of $k_T^{(\mathrm{i})}$. From Eq. (12), this behavior is attributed to the sharp decrease in ion temperature in the coronal region, while the electron temperature remains relatively stable, causing $k_T^{(\mathrm{e})}$ to rise with plasma evolution. Consequently, at later times, $k_T^{(\mathrm{e})}$ dominates the ion diffusive flux, playing the most significant role in governing the ion transport processes within the plasma. The sharp decline at the end of each diffusion coefficients plot is a direct consequence of the no-flux boundary conditions, which prevent any flow or diffusion across the boundaries.

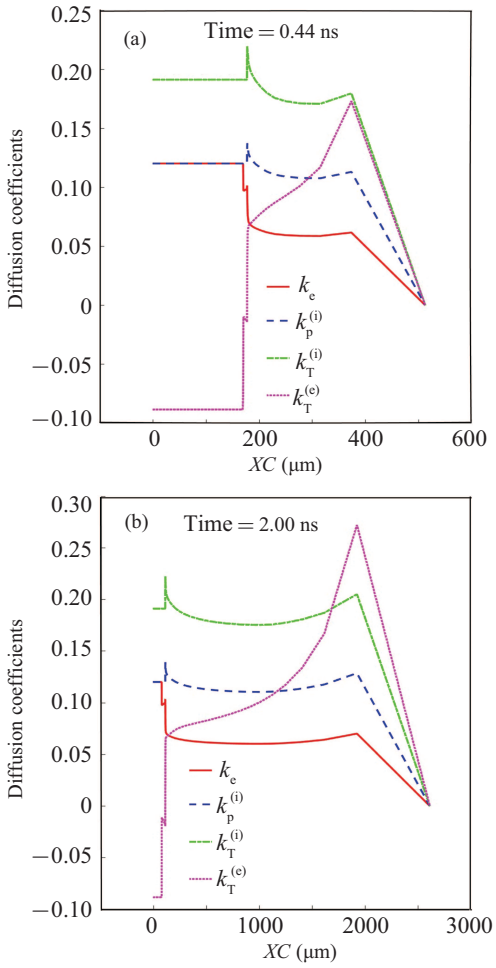


Fig. 5. Four normalized diffusion coefficients as a function of mass concentration for CH.

The contributions of various terms in the ion mass flux equation, plotted as a function of the target thickness (XC) in a laser-ablated plasma can be seen in Fig. 6. The flux equation is normalized with $\rho^2 D$. Each curve represents a distinct mechanism driving ion diffusion: concentration gradients ∇c_a, pressure gradients $k_p^{(\mathrm{i})}\nabla \ln P_{\mathrm{i}}$, thermal diffusion of ions $k_T^{(\mathrm{i})}\nabla \ln T_{\mathrm{i}}$, electron temperature gradients $k_T^{(\mathrm{e})}\nabla \ln T_{\mathrm{e}}$, and electrostatic diffusion $(ek_{\mathrm{e}}/T_{\mathrm{i}})\nabla\phi$. The net mass diffusive flux, i_{net}, shown as the red curve, represents the cumulative effect of all terms. As seen in the figure, the diffusive flux is dominated by the ion temperature gradient. The sharp peaks in i_{net} correspond to localized regions where multiple gradients overlap, indicating intense ion diffusion near the ablation front. This helps us to analyze the critical role of different gradients in determining ion diffusion dynamics.

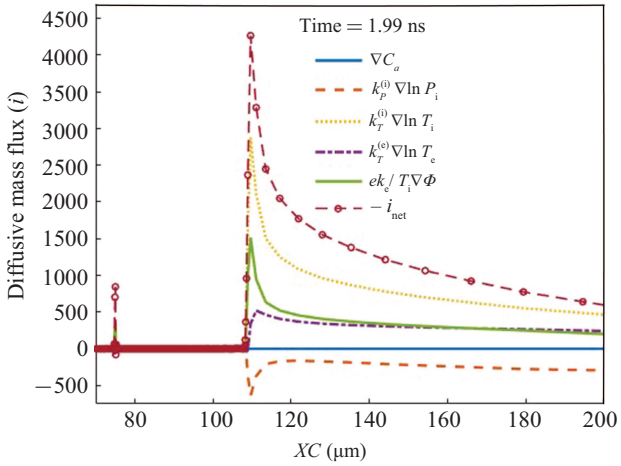


Fig. 6. Spatial profiles of ion mass flux contributions in laser-ablated CH target.

The temperature profiles of electrons (T_{e}) and ions (T_{i}) with and without considering mass concentration variations are shown in Fig. 7 during laser-driven ablation of CH material. It can be seen that the temperature difference for ions and electrons temperatures before and after considering ion component separation phenomenon is very small ($< 1\%$). As seen in Fig. 7(a), the electron temperature profile rises steeply near the critical density surface due to laser energy deposition via inverse bremsstrahlung, where electrons efficiently absorb energy due to their high mobility. Beyond this region, in the corona, the profile becomes nearly horizontal, demonstrating efficient energy transport through electron thermal conduction. The inset indicates minor variations between the new and old models, reflecting improvements in thermal conduction behavior in the updated model. As shown in Fig. 7(b), the ion temperature profile also peaks near the critical density but declines significantly in the coronal region. This is due to the reduced collisionality and weaker coupling with electrons, resulting in inefficient energy retention. The inset shows minor differences between the new and old models, showcasing improved ion dynamics modeling in the updated framework. The divergence between T_{e} and T_{i} is explained by the disparity in

their mass and transport properties, with electrons exhibiting higher thermal mobility compared to ions.

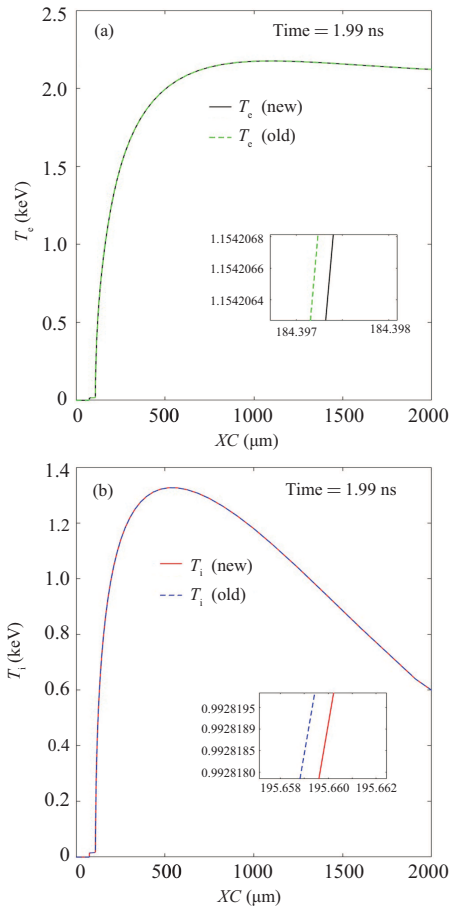


Fig. 7. The spatial distribution of electron and ion temperature profiles.

The pressure profiles of electrons (P_e) and ions (P_i) with and without mass diffusion effect are shown in Fig. 8. It shows the electron pressure (P_e) decreases smoothly with spatial evolution, starting from a peak near the critical density surface. This behavior reflects the energy transport and plasma expansion dynamics. The inset reveals slight differences between the new and old models, where the updated model predicts slightly higher pressures, indicating improved accuracy in modeling energy deposition. In Fig. 8(b), the ion pressure (P_i) also decreases with plasma expansion but exhibits a steeper decline compared to the electron pressure. This reflects the ions' lower energy transport efficiency and reduced collisionality in the expanding plasma. The inset shows subtle differences between the models, demonstrating the updated model's enhanced ability to simulate ion dynamics more accurately.

From Figs. 6–8, it can be seen that the temperature and pressure of electrons and ions changes drastically near the ablation surface which leads to the tendency of H ions to diffuse to the ablation surface. The light ions diffuse from the near-critical density region. Their tendency to move toward the ablation surface and low-density regions leads to variations in ion abundance, which is no longer constant. This behavior indicates the effects of ion diffusion and redistribution during plasma expansion.

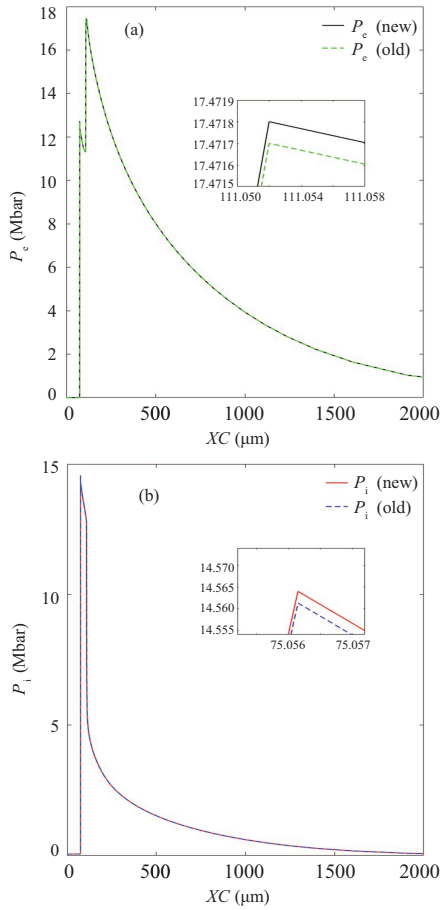


Fig. 8. The spatial distribution of electron and ion pressure profiles.

3.3. Impact of ion diffusion on CBET coupling factor

As we mentioned in Introduction, ion-species separation modifies the damping rate of ion-acoustic waves. To quantify the impact of ion diffusion on CBET gain, we employ the linear kinetic theory, where the damping rate is self-consistently included. In the energy transfer process, the CBET coupling factor K plays a critical role. The coupling factor, which quantifies the efficiency of energy transfer between laser beams in a plasma is given by[15]

$$K = \frac{\chi_e\,(1+\sum_a \chi_a)}{1+\chi_e+\sum_a \chi_a}, \tag{14}$$

where χ_e and χ_a represent the susceptibilities of electrons and ions respectively. When the plasma is in local quasi-equilibrium state, the susceptibilities can be described with the plasma dispersion function W,[14]

$$\chi_e = -\frac{1}{2(k\lambda_{De})^2} W'\left[\frac{\Delta\omega - \Delta\boldsymbol{k}\cdot\boldsymbol{u}_e}{\sqrt{2}kv_{T_e}}\right], \tag{15a}$$

$$\chi_a = -\frac{1}{2(k\lambda_{De})^2}\frac{T_e}{T_i}\sum_a \frac{Z_a^2 n_a}{n_e} W'\left[\frac{\Delta\omega - \Delta\boldsymbol{k}\cdot\boldsymbol{u}_a}{\sqrt{2}kv_{T_a}}\right]. \tag{15b}$$

Here $\Delta\boldsymbol{k}$ is the difference of wave vectors $\boldsymbol{k}_1$ and $\boldsymbol{k}_2$ for a pair of crossing laser beams and $\Delta\omega$ is their frequency difference; $\Delta\omega = \omega_1 - \omega_2$. Additionally, the bulk fluid velocity of

the plasma $\boldsymbol{u}$ is considered to contain the Doppler shift effect, where λ_{De} is the electron Debye length, $v_{T_e} = \sqrt{k_B T_e/m_e}$ is the electron thermal velocity and $v_{T_a} = \sqrt{k_B T_i/m_a}$ is ion thermal speed with k_B as Boltzmann constant.

The real part of K is associated with phase shifts and wave propagation characteristics but the imaginary part of K is directly related to the damping or growth of ion-acoustic waves, which govern the efficiency of CBET.[25]

The presented plots in Fig. 9 illustrate the variation of key parameters as a function of the spatial position using electron temperature T_e, ion temperature T_i, bulk fluid velocity $\boldsymbol{u}$, electron number density n_e, center of cells (target thickness) and ion concentration c_a from MULTI-1D data for four different cases, each characterized by a different wavelength difference of the incident laser beams ($\Delta\lambda$). The angel between the two laser beams is 40° and one of the laser beams has a wavelength of 0.351 μm. The black solid and dashed lines represent the coupling factor parameter K with and without diffusion, respectively, while the other curves depict additional relevant physical quantities (n_e, c_a). In case 1 ($\Delta\lambda = 0.87$ nm), the diffusion effect introduces a notable difference between the two coupling factors, particularly between ∼ 330 μm–1300 μm. In cases 2 and 3, the coupling factor K profiles shows a very small rather negligible difference near the ablation front. In case 4 ($\Delta\lambda = 1.3$ nm), the largest wavelength difference between the incident laser beams results in altered coupling factor profiles but the peak variation is not as large as in case 1. The separation of carbon (C) and hydrogen (H) ion components will significantly affect the damping rate of ion acoustic waves. This, in turn, influences the magnitude of the coupling strength (characterized by the density perturbation of ion acoustic waves) and the width of the resonance peak. Furthermore, in the presence of bulk velocity, variations in the damping rate due to component separation impact the size of the resonance region in CBET. This effect is demonstrated by the localized variation of the coupling factor K under conditions with and without ion diffusion. These findings emphasize the crucial role of ion diffusion in shaping the behavior of the coupling factor K and its dependence on the initial wavelength difference between the incident laser beams.

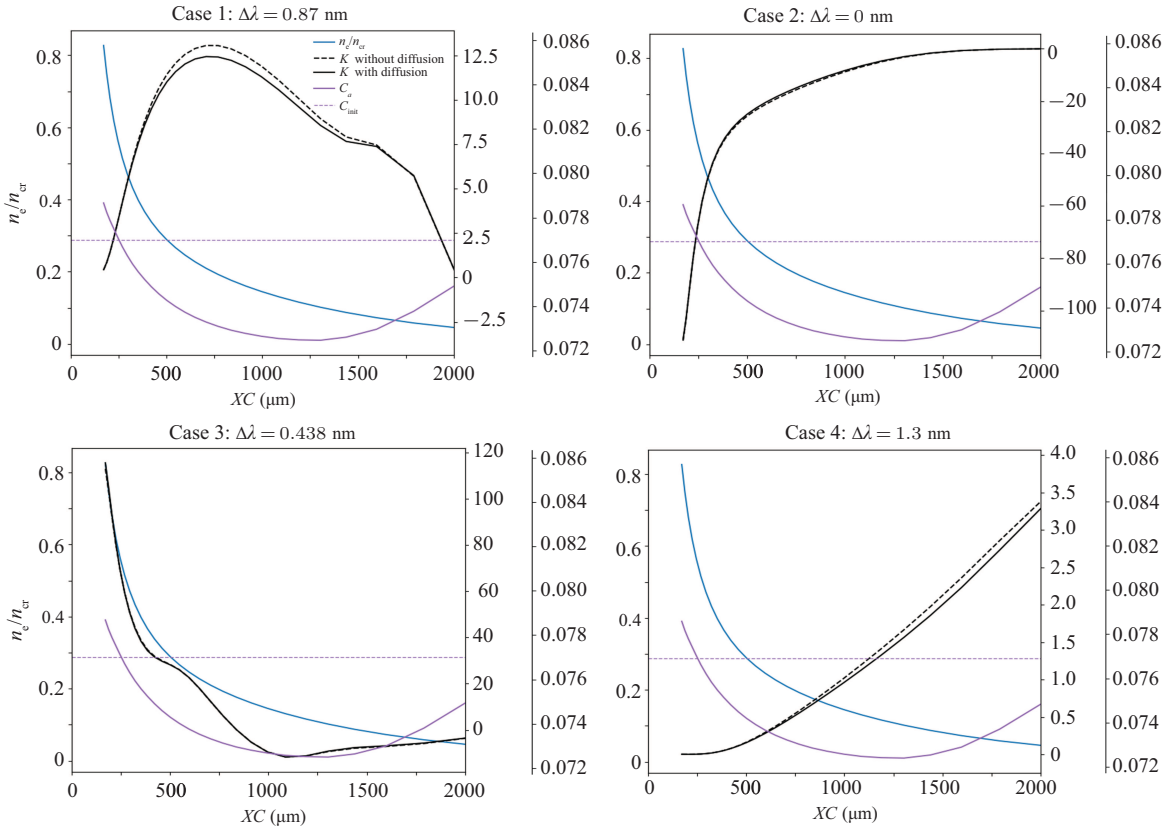


Fig. 9. Spatial variation of electron number density n_e, mass concentration C_a and CBET coupling factor K with and without ion diffusion for different spectral bandwidths $\Delta\lambda$.

4. Conclusion

In summary, we have used a set of ion diffusion equations in a systematic manner with Lagrangian coordinates and modified the MULTI-1D code. We have investigated the impact of incorporating ion diffusion model into the existing program of MULTI-1D for the study of laser-driven ablation of CH material. By extending the program to account for mass diffusion effects, we aimed to enhance the accuracy of thermodynamic predictions, including the electron and ion temperature (T_e and T_i) and pressure (P_e and P_i) profiles. The analysis demonstrates that the inclusion of ion diffusion for a planar target geometry, introduces only minor modifications to the electron

and ion temperature and pressure profiles along with the mass density distributions. But a noticeable impact on CBET coupling factor was observed with the change in ion abundance for a specific initial wavelength difference of the incident laser beams, which is very important in energy transfer mechanism (CBET). The updated model reflects slight refinements in the equations of state (EOS) due to the enhanced treatment of ion transport phenomena. The variations observed in T_e and T_i are minimal, indicating that the plasma behavior remains dominated by the primary energy transport mechanisms, while ion diffusion provides a secondary correction. Similarly, the electron and ion pressure profiles exhibit very small differences between the new and previous models, as shown in the insets of the presented plots. While, the ion concentration variation affects the damping rate of ion acoustic waves, altering coupling strength K, resonance peak width, and the size of the CBET resonance region. The results also show that the coupling factor is highly localized around a specific mass concentration indicating a specific mass concentration is optimal for CBET. Our analysis indicates that while ion diffusion exerts a limited influence on overall plasma dynamics, its effects are non-negligible, particularly in fusion experiments where precision is critical. This study focuses on a planar target geometry; however, in spherical implosion scenarios relevant to inertial confinement fusion, especially during the thermonuclear phase where mass diffusivity increases significantly (scaling approximately as $\mathcal{O}(T^{2.5})$), ion diffusion may substantially affect both mechanical and thermal plasma states. These effects, including potential interactions with plasma turbulence,[26] warrant further investigation in future work.

Appendix A: Numerical implementation

For simulations specie specific EOS and ionization tables are used from FEOS and similarly opacity tables are used from TOPS. These tables are generated under real-time conditions to ensure fidelity to physical processes. A mass concentration vector (c_a) has been defined and integrated within the `typesimstate` structure. This vector stores the concentration of species at each computational point. The derivatives of thermodynamic properties with respect to mass concentration, namely $\partial T_e/\partial c$, $\partial T_i/\partial c$, $\partial P_e/\partial c$, and $\partial P_i/\partial c$, have been included in the `typesimthermo` structure. These derivatives are crucial for modeling the evolution of plasma properties under varying species concentrations. The initial concentration of each species is computed in the `init_state` subroutine. For example, for CH, the mass concentration of carbon is initialized as

$$c_a = \frac{\rho_a}{\rho_a + \rho_b}, \tag{A1}$$

where ρ_a and ρ_b are the mass fraction of hydrogen and carbon, respectively. A comprehensive model to calculate the evolution of mass concentration and its impact on plasma characteristics (e.g., ion and electron temperatures and pressures) has been implemented using our ion diffusion equations. This model is integrated into the main simulation workflow. Specifically, it is invoked in the `SCHRITT` subroutine after the `EOS` subroutine. This is one of the main subroutine and it performs a time step. It uses time segmentation and all physical processes are carried out individually, one by one in this subroutine. This sequence ensures that the updated mass concentration values are reflected in subsequent calculations of plasma properties. The integrate subroutine updates the initial values of the parameters and updates the new values over time. It also calls step subroutine which further has `schritt` subroutine in which most of the physical models have been called including our new model for ion diffusion. The `schritt` subroutine is a critical component of the simulation code, responsible for handling the time evolution of the simulation state over a single time step (`dt`). It operates by iterating through sub-cycles to ensure stability and accuracy while incorporating multiple physical processes to simulate laser-driven plasma.

The subroutine updates the simulation state (`s2`) based on the input parameters (`p`), initial state (`s1`), and energy contributions (`e`) over a specified time step. It ensures consistent handling of thermodynamics, energy deposition, and transport. The `schritt` subroutine is a critical component of the simulation, responsible for integrating multiple physical processes that govern laser–plasma interactions. It begins with an initialization phase, where memory is allocated for auxiliary structures (`typesimstate` and `typesimthermo`), and local variables are initialized which ensures the computational framework is ready for subsequent calculations. The subroutine also includes a sub-cycle loop, where key processes such as thermodynamic updates, mass concentration dynamics, laser energy deposition, and hydrodynamics are performed. These calculations involve using equation-of-state (EOS) tables to compute plasma properties like pressure, temperature, and ionization. Other aspects include simulating heat transport, radiation fluxes, and monitoring stability through critical parameter variations. In the final phase, the subroutine advances the simulation time, updates the energy partitioning, and transfers the updated state back to the main simulation.

Appendix B: Ion–ion thermal force coefficients

In this section, we present the set of matrix equations and relevant matrices for calculating the ion–ion thermal force coefficients $h_0^{(a)}$ and $g_0^{(a)}$ which satisfy a system of linear equations. These matrix equations account for interactions between ion species of types a and b. The collision matrix elements were solved using the method of generating function expansion and applying the Enskog conditions to a system of linear equations. In the below matrix equations, the index n ranges

from 0 to 2, inclusive.

$$HV = R, \quad V = H^{-1}R, \tag{B1}$$

where

$$V = \begin{pmatrix} h_0^{(a)} \\ h_1^{(a)} \\ h_2^{(a)} \\ h_0^{(b)} \\ h_1^{(b)} \\ h_2^{(b)} \end{pmatrix}, \quad R = \begin{pmatrix} 0 \\ -5/4 \\ 0 \\ 0 \\ -5/4 \\ 0 \end{pmatrix}.$$

Similarly,

$$GI = Q, \quad I = G^{-1}Q, \tag{B2}$$

where

$$I = \begin{pmatrix} g_0^{(a)} \\ g_1^{(a)} \\ g_2^{(a)} \\ g_0^{(b)} \\ g_1^{(b)} \\ g_2^{(b)} \end{pmatrix}, \quad Q = \begin{pmatrix} 0 \\ 0 \\ 0 \\ \dfrac{(1-c_a)m_a + c_a m_b}{2(1-c_a)m_a} \\ 0 \\ 0 \end{pmatrix}$$

For two-ion species, thermal force coefficient matrices G and H for the cut off value of $n = 2$ are given below:

$$H = \begin{bmatrix} A_1 & A_2 & A_3 & B_1 & B_2 & B_3 \\ A_4 & A_5 & A_6 & B_4 & B_5 & B_6 \\ A_7 & A_8 & A_9 & B_7 & B_8 & B_9 \\ C_1 & C_2 & C_3 & D_1 & D_2 & D_3 \\ C_4 & C_5 & C_6 & D_4 & D_5 & D_6 \\ C_7 & C_8 & C_9 & D_7 & D_8 & D_9 \end{bmatrix}, \tag{B3}$$

where the matrix elements of H can be simplified as below:

$$A_1 = c_a^2\mu^{3/2}, \quad A_2 = 0, \quad A_3 = 0, \quad A_4 = -\frac{3}{4}\left(\frac{\mu}{1+\mu}\right)^{3/2},$$

$$A_5 = -\frac{1}{8}\frac{\sqrt{\mu}(30+16\mu+13\mu^2)}{(1+\mu)^{5/2}} - \frac{\sqrt{2}c_a\mu Z_{ab}^2}{2(1-c_a)}, \quad A_6 = -\frac{3}{32}\frac{\mu^{3/2}(84+32\mu+23\mu^2)}{(1+\mu)^{7/2}} - \frac{3\sqrt{2}c_a\mu Z_{ab}^2}{8(1-c_a)},$$

$$A_7 = -\frac{15}{16}\frac{\mu^{5/2}}{(1+\mu)^{5/2}}, \quad A_8 = -\frac{2}{32}\frac{\mu^{3/2}(84+32\mu+23\mu^2)}{(1+\mu)^{7/2}} - \frac{3\sqrt{2}\mu Z_{ab}^2}{8(1-c_a)},$$

$$A_9 = -\frac{1}{128}\frac{\sqrt{\mu}(1400+1792\mu+3672\mu^2+1088\mu^3+433\mu^4)}{(1+\mu)^{9/2}} - \frac{45\sqrt{2}c_a\mu Z_{ab}^2}{32(1-c_a)},$$

$$B_1 = (1-c_a)^2, \quad B_2 = 0, \quad B_3 = 0, \quad B_4 = \frac{3}{4}\frac{(1-c_a)\mu}{c_a(1+\mu)^{5/2}},$$

$$B_5 = \frac{27}{8}\frac{(1-c_a)}{c_a(1+\mu)^{5/2}}, \quad B_6 = \frac{225}{32}\frac{(1-c_a)\mu}{c_a(1+\mu)^{5/2}}, \quad B_7 = \frac{15}{16}\frac{(1-c_a)\mu}{c_a(1+\mu)^{5/2}},$$

$$B_8 = \frac{225}{32}\frac{(1-c_a)\mu}{c_a(1+\mu)^{5/2}}, \quad B_9 = \frac{2625}{128}\frac{(1-c_a)\mu^2}{c_a(1+\mu)^{5/2}}$$

$$C_1 = \frac{1}{2}\frac{c_a\sqrt{\mu}(1+2\mu+\mu^2)}{(1-c_a)\mu^2(1+\mu)^{5/2}}, \quad C_2 = \frac{3}{4}\frac{c_a}{(1-c_a)\mu(1+\mu)^{3/2}}, \quad C_3 = \frac{15}{16}\frac{c_a}{(1-c_a)(1+\mu)^{5/2}},$$

$$C_4 = \frac{3}{4}\frac{c_a}{(1-c_a)(1+\mu)^{3/2}}, \quad C_5 = \frac{27}{8}\frac{c_a}{(1-c_a)}\left(\frac{\mu}{1+\mu}\right)^{5/2}, \quad C_6 = \frac{225}{32}\frac{c_a}{(1-c_a)}\left(\frac{\mu}{1+\mu}\right)^{7/2},$$

$$C_7 = \frac{15}{16}\frac{c_a}{(1-c_a)}\left(\frac{\mu}{1+\mu}\right)^{5/2}, \quad C_8 = \frac{225}{32}\frac{c_a}{(1-c_a)}\left(\frac{\mu}{1+\mu}\right)^{7/2}, \quad C_9 = \frac{2625}{128}\frac{c_a}{(1-c_a)}\left(\frac{\mu}{1+\mu}\right)^{9/2},$$

$$D_1 = -\frac{1}{2\sqrt{1+\mu}}, \quad D_2 = -\frac{3}{4}\left(\frac{1}{1+\mu}\right)^{3/2}, \quad D_3 = -\frac{15}{16}\left(\frac{1}{1+\mu}\right)^{5/2},$$

$$D_4 = -\frac{3}{4}\left(\frac{1}{1+\mu}\right)^{3/2}, \quad D_5 = -\frac{(13+16\mu+30\mu^2)}{8}\left(\frac{1}{1+\mu}\right)^{5/2} - \frac{\sqrt{2}(1-c_a)}{2c_a\mu Z_{ab}^2},$$

$$D_6 = -\frac{3}{32}\frac{(23+32\mu+84\mu^2)}{(1+\mu)^{7/2}} - \frac{3\sqrt{2}(1-c_a)}{8c_a\mu {Z_{ab}}^2}, \quad D_7 = -\frac{15}{16(1+\mu)^{5/2}},$$

$$D_8 = -\frac{3}{32}\frac{(23+32\mu+84\mu^2)}{(1+\mu)^{7/2}} - \frac{3\sqrt{2}(1-c_a)}{8c_a\mu {Z_{ab}}^2},$$

$$D_9 = -\frac{1}{128}\frac{(433+1088\mu+3672\mu^2+1792\mu^3+1400\mu^4)}{(1+\mu)^{9/2}} - \frac{45\sqrt{2}(1-c_a)}{32c_a\mu Z_{ab}^2},$$

additionally,

$$G = \begin{bmatrix} U_1 & U_2 & U_3 & V_1 & V_2 & V_3 \\ U_4 & U_5 & U_6 & V_4 & V_5 & V_6 \\ U_7 & U_8 & U_9 & V_7 & V_8 & V_9 \\ W_1 & W_2 & W_3 & X_1 & X_2 & X_3 \\ W_4 & W_5 & W_6 & X_4 & X_5 & X_6 \\ W_7 & W_8 & W_9 & X_7 & X_8 & X_9 \end{bmatrix}, \tag{B4}$$

where the relevant matrix elements are given below:

$$U_1 = c_a^2\mu^{3/2}, \quad U_2 = 0, \quad U_3 = 0, \quad U_4 = -\frac{3\mu^{3/2}}{4(1+\mu)^{3/2}},$$

$$U_5 = -\frac{1}{8}\frac{(30+16\mu+13\mu^2)}{\sqrt{\mu}(1+\mu)^{5/2}} - \frac{\sqrt{2}c_a\mu Z_{ab}^2}{2(1-c_a)}, \quad U_6 = -\frac{3}{32}\frac{\mu^{3/2}(84+32\mu+23\mu^2)}{(1+\mu)^{7/2}} - \frac{3\sqrt{2}c_a\mu Z_{ab}^2}{8(1-c_a)},$$

$$U_7 = -\frac{15}{16}\left(\frac{\mu}{1+\mu}\right)^{5/2}, \quad U_8 = -\frac{3}{32}\frac{\mu^{3/2}(84+32\mu+23\mu^2)}{(1+\mu)^{7/2}} - \frac{3\sqrt{2}c_a\mu Z_{ab}^2}{8(1-c_a)},$$

$$U_9 = -\frac{1}{128}\frac{\sqrt{\mu}(1400+1792\mu+3672\mu^2+1088\mu^3+433\mu^4)}{(1+\mu)^{9/2}} - \frac{45\sqrt{2}c_a\mu Z_{ab}^2}{32(1-c_a)},$$

$$V_1 = -(1-c_a)^2, \quad V_2 = 0, \quad V_3 = 0, \quad V_4 = -\frac{3}{4}\frac{(1-c_a)}{c_a(1+\mu)^{3/2}},$$

$$V_5 = -\frac{27}{28}\frac{(1-c_a)}{c_a(1+\mu)^{5/2}}, \quad V_6 = -\frac{225}{32}\frac{(1-c_a)}{c_a(1+\mu)^{7/2}},$$

$$V_7 = -\frac{15}{16}\frac{(1-c_a)\mu}{c_a(1+\mu)^{5/2}}, \quad V_8 = -\frac{225}{32}\frac{(1-c_a)\mu}{c_a(1+\mu)^{7/2}}, \quad V_9 = -\frac{2625}{128}\frac{(1-c_a)\mu}{c_a(1+\mu)^{9/2}},$$

$$W_1 = -\frac{1}{2}\frac{c_a\mu^{5/2}}{(1-c_a)(1+\mu)^{1/2}}, \quad W_2 = -\frac{3}{4}\frac{c_a\mu^{5/2}}{(1-c_a)(1+\mu)^{3/2}}, \quad W_3 = -\frac{15}{16}\frac{c_a\mu^{7/2}}{(1-c_a)(1+\mu)^{5/2}},$$

$$W_4 = -\frac{3}{4}\frac{c_a\mu^{5/2}}{(1-c_a)(1+\mu)^{3/2}}, \quad W_5 = -\frac{27}{8}\frac{c_a\mu^{5/2}}{(1-c_a)(1+\mu)^{5/2}}, \quad W_6 = -\frac{225}{32}\frac{c_a\mu^{7/2}}{(1-c_a)(1+\mu)^{7/2}},$$

$$W_7 = -\frac{15}{16}\frac{c_a\mu^{5/2}}{(1-c_a)(1+\mu)^{5/2}}, \quad W_8 = -\frac{225}{32}\frac{c_a\mu^{5/2}}{(1-c_a)(1+\mu)^{7/2}}, \quad W_9 = -\frac{2625}{128}\frac{c_a\mu^{7/2}}{(1-c_a)(1+\mu)^{9/2}},$$

$$X_1 = -\frac{1}{2\sqrt{1+\mu}}, \quad X_2 = -\frac{3}{4}\left(\frac{1}{1+\mu}\right)^{3/2}, \quad X_3 = -\frac{15}{16}\left(\frac{1}{1+\mu}\right)^{5/2},$$

$$X_4 = -\frac{3}{4}\left(\frac{1}{1+\mu}\right)^{3/2}, \quad X_5 = -\frac{(13+16\mu+30\mu^2)}{8}\left(\frac{1}{1+\mu}\right)^{5/2} - \frac{\sqrt{2}(1-c_a)}{2c_a\mu Z_{ab}^2},$$

$$X_6 = -\frac{3}{32}\frac{(23+32\mu+84\mu^2)}{(1+\mu)^{7/2}} - \frac{3\sqrt{2}(1-c_a)}{8c_a\mu Z_{ab}^2}, \quad X_7 = -\frac{15}{16(1+\mu)^{5/2}},$$

$$X_8 = -\frac{3(23+32\mu+84\mu^2)}{32\mu^{3/2}(1+\mu)^{7/2}} - \frac{3\sqrt{2}(1-c_a)}{8c_a\mu Z_{ab}^2},$$

$$X_9 = -\frac{1}{128}\frac{(433+1088\mu+3672\mu^2+1792\mu^3+1400\mu^4)}{(1+\mu)^{9/2}} - \frac{45\sqrt{2}(1-c_a)}{32c_a\mu Z_{ab}^2},$$

where $\mu = m_b/m_a$ having m_a, m_b, and Z_{ab} representing the masses of a and b ions, and their atomic number ratio $Z_{ab} = Z_a/Z_b$, respectively. Hence, by putting the respective values in Eqs. (B1) and (B2), the ion-ion thermal force coefficients $h_0^{(a)}$ and $g_0^{(a)}$ can easily be calculated.

Acknowledgments

Project supported by the National Nature Science Foundation of China (Grant No. 12375242) and the Strategic Priority Research Program of the Chinese Academy of Sciences (Grant No. XDA25010200). We would also like to thank Mr. Lu, a former graduate student, for his contribution in deriving

the analytical expressions that we have used in our theoretical framework.

References

[1] Atzeni S and Meyer-ter Vehn J 2004 *The Physics of Inertial Fusion: Beam Plasma Interaction, Hydrodynamics, Hot Dense Matter* (Clarendon Press)

[2] Lindl J 1995 *Phys. Plasmas* **2** 3933

[3] Lindl J D, Amendt P, Berger R L, Glendinning S G, Glenzer S H, Haan S W, Kauffman R L, Landen O L and Suter L J 2004 *Phys. Plasmas* **11** 339

[4] Craxton R, Anderson K, Boehly T, Goncharov V, Harding D, Knauer J, McCrory R, McKenty P, Meyerhofer D, Myatt J, *et al.* 2015 *Phys. Plasmas* **22** 11

[5] Landau L D and Lifshitz E M 1987 *Fluid Mechanics*, 2nd edn. (Pergamon Press)

[6] Kagan G and Tang X Z 2012 *Phys. Plasmas* **19** 8

[7] Hu S X, Fiksel G, Goncharov V N, Skupsky S, Meyerhofer D D and Smalyuk V A 2012 *Phys. Rev. Lett.* **108** 195003

[8] Fiksel G, Hu S X, Goncharov V A, Meyerhofer D D, Sangster T C, Smalyuk V A, Yaakobi B, Bonino M J and Jungquist R 2012 *Phys. Plasmas* **19** 062704

[9] Zheng G, Tao T, Jia Q, Yan R and Zheng J 2022 *Plasma Physics and Controlled Fusion* **64** 105003

[10] Williams E A, Berger R L, Drake R P, Rubenchik A M, Bauer B S, Meyerhofer D D, Gaeris A C and Johnston T W 1995 *Phys. Plasmas* **2** 129

[11] Neumayer P, Berger R L, Divol L, Froula D H, London R A, MacGowan B J, Meezan N B, Ross J S, Sorce C, Suter L J and Glenzer S H 2008 *Phys. Rev. Lett.* **100** 105001

[12] Glenzer S H, MacGowan B J, Michel P, *et al.* 2010 *Science* **327** 1228

[13] Kritcher A L, Zylstra A B, Weber C R, *et al.* 2024 *Phys. Rev. E* **109** 25204

[14] Michel P, Rozmus W, Williams E A, Divol L, Berger R L, Glenzer S H and Callahan D A 2013 *Phys. Plasmas* **20** 5

[15] Michel P 2023 *Introduction to laser-plasma interactions* (Springer Nature)

[16] Ramis R and Meyer-ter Vehn J 2016 *Comput. Phys. Commun.* **203** 226

[17] Ramis R, Eidmann K, Meyer-ter Vehn J and Hüller S 2012 *Comput. Phys. Commun.* **183** 637

[18] Hsu S C, Joshi T R, Hakel P, Vold E L, Schmitt M J, Hoffman N M, Rauenzahn R M, Kagan G, Tang X Z, Mancini R C, *et al.* 2016 *Europhys. Lett.* **115** 65001

[19] Joshi T R, Hakel P, Hsu S C, Vold E L, Schmitt M J, Hoffman N M, Rauenzahn R M, Kagan G, Tang X Z, Mancini R, *et al.* 2017 *Phys. Plasmas* **24**

[20] Joshi T R, Hsu S C, Hakel P, Hoffman N M, Sio H and Mancini R 2019 *Phys. Plasmas* **26**

[21] Lu Y J, Tao T, Zhao B and Zheng J 2023 *Acta Phys. Sin.* **72** 075201 (in Chinese)

[22] Kagan G and Tang X Z 2014 *Phys. Lett. A* **378** 1531

[23] Faik S, Tauschwitz A and Iosilevskiy I 2018 *Comput. Phys. Commun.* **227** 117

[24] Abdallah J Jr and Clark R E 1985 *Tops: A multigroup opacity code*, Tech. Rep. Los Alamos National Lab., NM (USA)

[25] Williams E, Berger R, Drake R, Rubenchik A, Bauer B, Meyerhofer D, Gaeris A and Johnston T 1995 *Phys. Plasmas* **2** 129

[26] Weber C, Clark D, Cook A, Busby L and Robey H 2014 *Phys. Rev. E* **89** 053106